PHYSICAL REVIEW B **110**, 094105 (2024)

Interpretation of phonon spectroscopic data at atomic resolution in scanning transmission electron microscopy

Juri Barthel[1,*] and Leslie J. Allen[2,†]
[1]*Ernst Ruska-Centre (ER-C 2) Forschungszentrum Juelich GmbH, 52425 Juelich, Germany*
[2]*School of Physics, University of Melbourne, Parkville VIC 3010, Australia*

(Received 26 June 2024; revised 28 August 2024; accepted 4 September 2024; published 13 September 2024)

We provide a theory for atomic resolution phonon spectroscopy in scanning transmission electron microscopy. This formulation goes beyond a recently proposed simple approach to atomic-scale phonon spectroscopy by explicitly including the dependence on probe position in the inelastic scattering cross section itself and considers the contribution to the spectrum from individual atoms. An application is made to existing experimental data that demonstrates how a direct comparison of the data with phonon densities of states projected onto individual atoms can be made and also the importance of contributions to the energy-loss spectrum on a particular atomic site from surrounding atoms due to probe spreading.

DOI: 10.1103/PhysRevB.110.094105

I. INTRODUCTION

Monochromated electron sources have facilitated the characterization of the vibrational states of materials at the atomic scale using electron energy-loss spectroscopy (EELS) in scanning transmission electron microscopy (STEM) [1]. Several experiments have been carried out, mainly on thin samples containing light elements, for example Refs. [2–13]. Thicker specimens containing heavier elements have also been examined using STEM phonon EELS, for example Refs. [14–16]. A variety of approaches have been employed to understand the underlying physics of the experimental results [2,8,10,17–28]. The relationship between a subset of these approaches was explored in a paper by Zeiger *et al.* [29] and the importance of being able to correctly account for the channeling (multiple elastic scattering of the probing electrons), particularly in the case of thicker specimens, was pointed out.

A simple approach to simulating the phonon sector in EELS was recently proposed [30]. The physics encapsulated in the dispersion curves, due to correlated motion of the atoms, was incorporated in an integrated way via the phonon density of states (PDOS), which is a function of phonon energy. For a given PDOS, a spectral distribution function was derived and this function distributes the total inelastic phonon scattering, which can be calculated using the quantum excitation of phonons model [20], into an energy-loss and gain spectrum. The usefulness of this approach was illustrated in the case of silicon. This model does not predict any variation of the shape of the spectrum as one scans the probe across columns containing different elements, whereas that introduced here does.

The approach in this paper explicitly includes the dependence on probe position in the inelastic scattering cross section itself and considers the contribution to the spectrum from individual atoms. This allows for a change of shape in the spectrum as a function of probe position for specimens containing different atomic species. The advantages of the model presented here will be demonstrated by its application to the pioneering recent work of Xu *et al.* [13] addressing single-atom vibrational spectroscopy with chemical-bonding sensitivity for graphene containing Si and N impurities. This example will show how the theory presented facilitates comparison of energy-loss spectra and the PDOS and how one might deduce the PDOS projected on individual atoms from STEM EELS recorded with atomic-scale resolution. The ability to access the projected PDOS at an atomic level experimentally and compare the data to theoretical models, at the same level, extends what is possible using the usual approaches to measure the overall PDOS of a sample by inelastic neutron scattering, which is averaged over large volumes [31].

II. THEORY

A. Inelastic scattering cross section

We take as our starting point the following equation describing an inelastic scattering event that occurs at a specific depth z_i into the specimen [32–34], measured from the entrance surface of the specimen and along the optical axis:

$$\psi_n(\mathbf{R},\mathbf{r},z_i) = -i\sigma_n H_{n0}(\mathbf{r},z_i)\psi_0(\mathbf{R},\mathbf{r},z_i). \tag{1}$$

The wave function ψ_0 incident on the slice at the depth z_i depends on the coordinate $\mathbf{r}$ in a plane perpendicular to the optical axis. The functional dependence denoted by $\mathbf{R}$ specifies the probe position on the surface of the specimen. The *projected* inelastic transition potential H_{n0} describes an inelastic phonon transition, via a Coulomb interaction, at the depth z_i from an initial state of the specimen labeled 0 to a final state labeled n and, for an incident plane wave, its modulus squared gives the probability that that transition will occur [33]. Here

---

[*] Contact author: ju.barthel@fz-juelich.de

[†] Contact author: lja@unimelb.edu.au

$\sigma_n = m/2\pi\hbar^2 k_n$ is the interaction constant for the fast electron after energy loss, in which m is the relativistic mass of the electron and k_n is the wave number of the fast electron after the inelastic transition.

After an inelastic transition has occurred, the wave function of the fast electron can be considered to be one of the final states in the set $\{\psi_n\}$. Not only is the energy of the fast electron probe reduced by the inelastic scattering but, since the transition potential $H_{n0}(\mathbf{r}, z_i)$ is complex, the amplitude and phase of the wave function also changes. Fourier transforming Eq. (1) we obtain

$$\Psi_n(\mathbf{R}, \mathbf{g}, z_i) = -i\sigma_n \int H_{n0}(\mathbf{r}, z_i)\psi_0(\mathbf{R}, \mathbf{r}, z_i) e^{-2\pi i \mathbf{g}\cdot\mathbf{r}} d\mathbf{r}. \quad (2)$$

Now let us discuss scanning transmission electron microscopy. There is no post specimen imaging lens; instead a detector (spectrometer) is positioned in the far-field diffraction plane. We note that for a large enough acceptance angle on the detector, the subtleties due to the subsequent channelling of the inelastically scattered electron are integrated over [35,36] and a similar result can be obtained via a free space propagation to the detector. In that case the wave function in the diffraction (detector) plane is given directly by Eq. (2). The recorded signal (scattering cross section) is obtained by taking the modulus squared, multiplying by a current conversion factor k_n/k_0 [37], taking into account the pertinent final states, and integrating over the appropriate detector aperture D in the diffraction plane. This yields

$$I(\mathbf{R}, z_i) = \sum_{n\neq 0} \sigma_n^2 \frac{k_n}{k_0} \iint \Psi_0^*(\mathbf{R}, \mathbf{h}, z_i)\Psi_0(\mathbf{R}, \mathbf{g}, z_i) \times \int_{\mathrm{D}} H_{n0}^*(\mathbf{q}-\mathbf{h}, z_i) H_{n0}(\mathbf{q}-\mathbf{g}, z_i)\, d\mathbf{q}\, d\mathbf{h}\, d\mathbf{g}, \quad (3)$$

where the transition potentials in Eq. (2) have been Fourier transformed. For phonon excitation, $k_n \approx k_0$, which will be used later.

Ignoring the post transition channeling, the total signal from inelastic transitions at different depths z_i is the incoherent sum

$$I(\mathbf{R}) = \sum_i I(\mathbf{R}, z_i). \quad (4)$$

Let us briefly consider what all this means for phonon excitation. We consider a slice at depth z_i over which we must calculate the projected transition potentials $H_{n0}(\mathbf{q}, z_i)$ for all pertinent final states for a range of energy losses for the fast electron. Then we incoherently sum the contributions from all slices in the specimen. However, without further loss of generality, we will focus on a particular slice and, in what follows, we will drop writing the explicit dependence on z_i.

B. Transition potentials for phonon excitation

A transition potential describing inelastic phonon scattering can be written in the reciprocal space as a function of the scattering vector $\mathbf{q}$ as [20,22,24]

$$H_{\mathbf{n}0}(\mathbf{q}) = \frac{h^2}{2\pi m} \sum_\kappa \mathrm{e}^{-2\pi i \mathbf{q}\cdot\mathbf{R}_\kappa} f_{\mathrm{e}}^\kappa(\mathbf{q}) \times \prod_j \frac{\left[-i\sqrt{\frac{\pi h}{m_\kappa \omega_j}}\boldsymbol{\varepsilon}_j^\kappa\cdot\mathbf{q}\right]^{n_j}}{\sqrt{n_j!}} \mathrm{e}^{-\frac{\pi h}{2m_\kappa\omega_j}(\boldsymbol{\varepsilon}_j^\kappa\cdot\mathbf{q})^2}, \quad (5)$$

where the sum is over all atoms κ in the supercell with masses m_κ at positions $\mathbf{R}_\kappa$ and with electron scattering factors $f_{\mathrm{e}}^\kappa(\mathbf{q})$. The (real) polarization vectors per atom κ and for each normal mode j of the lattice dynamical eigenvalue problem are denoted by $\boldsymbol{\varepsilon}_j^\kappa$. The index j enumerates all phonon wave vectors in one half of the first Brillouin zone and, for each of these wave vectors, the pertinent branches of the dispersion relations in two classes of normal modes [19]. The prefactor before the summation contains the relativistic mass m of the probing electron. Equation (5) describes an excitation from the ground state to an excited state with quantum numbers n_j (elements of the vector $\mathbf{n}$, previously labeled simply with the generic index n) at phonon frequencies ω_j [24].

We assume that it suffices to consider only single phonon excitations, i.e., excitations where only one of the quantum numbers n_j equals 1, e.g., $n_{j'} = 1$, and the others are zero. Equation (5) then simplifies to

$$H_{(1j')0}(\mathbf{q}) = \frac{h^2}{2\pi m} \sum_\kappa \mathrm{e}^{-2\pi i \mathbf{q}\cdot\mathbf{R}_\kappa} f_{\mathrm{e}}^\kappa(\mathbf{q}) \times \left[-i\sqrt{\frac{\pi h}{m_\kappa \omega_{j'}}}\boldsymbol{\varepsilon}_{j'}^\kappa\cdot\mathbf{q}\right] \prod_j \mathrm{e}^{-\frac{\pi h}{2m_\kappa\omega_j}(\boldsymbol{\varepsilon}_j^\kappa\cdot\mathbf{q})^2}, \quad (6)$$

where the label $1j'$ indicates that the final state includes a single excitation of only the j'th mode. The product of exponentials at the end of the second line in Eq. (6) is the well-known Debye-Waller factor (DWF), which is often simplified further by assuming that the system is effectively isotropic. Explicitly, we have

$$\prod_j \mathrm{e}^{-\frac{\pi h}{2m_\kappa\omega_j}(\boldsymbol{\varepsilon}_j^\kappa\cdot\mathbf{q})^2} = \exp\left[-\frac{\pi h}{2m_\kappa}\sum_j \frac{1}{\omega_j}(\boldsymbol{\varepsilon}_j^\kappa\cdot\mathbf{q})^2\right] \approx \exp\left(-2\pi^2 q^2 \langle u_x^2\rangle^\kappa\right) = \exp(-B^\kappa q^2/4), \quad (7)$$

with $q = |\mathbf{q}|$, $\langle u_x^2\rangle^\kappa$ the mean square displacement (MSD) of atom κ along one dimension and B^κ the temperature factor. The second line assumes approximate isotropy. Equation (7) implicitly assumes that the system is initially at absolute zero, i.e., $T = 0\,\mathrm{K}$, and the motion parameterized by the MSD is due to the zero-point energy. We will consider temperatures $T > 0\,\mathrm{K}$ later. It is convenient in what follows to absorb the DWF and the factor $1/\sqrt{m_\kappa}$ in the term preceding the DWF in Eq. (6) into the electron scattering factors and define

$$\tilde{f}_e^\kappa(\mathbf{q}) = f_e^\kappa(\mathbf{q}) \exp(-B^\kappa q^2/4)/\sqrt{m_\kappa}. \quad (8)$$

C. Cross section and PDOS

We now make the approximation that cross terms between atoms can be ignored, i.e., we assume that the atoms in the specimen contribute to the energy-loss spectrum incoherently. This approximation can be justified in the case of STEM, where the electron probe mainly illuminates a single atom so that cross terms are expected to be small. The products of transition potentials in Eq. (3) can then be written, using Eqs. (6)–(8), in the form

$$\begin{aligned} &H^{*}_{(1j')0}(\mathbf{q}-\mathbf{h})H_{(1j')0}(\mathbf{q}-\mathbf{g}) \\ &\quad= \frac{h^4}{4\pi^2 m^2}\sum_{\kappa}\exp[-2\pi i(\mathbf{g}-\mathbf{h})\cdot\mathbf{R}_{\kappa}]\tilde{f}^{\kappa}_{e}(\mathbf{q}-\mathbf{h})\tilde{f}^{\kappa}_{e}(\mathbf{q}-\mathbf{g}) \\ &\quad\times\frac{\pi h}{2\omega_{j'}}\big[(\mathbf{q}-\mathbf{h})\cdot\boldsymbol{\varepsilon}^{\kappa}_{j'}\big]\big[(\mathbf{q}-\mathbf{g})\cdot\boldsymbol{\varepsilon}^{\kappa}_{j'}\big] \end{aligned} \tag{9}$$

and where effectively one of the terms in the sum over atoms κ dominates, depending on which atom is mainly illuminated by the atomic-scale STEM probe.

In addition to the above, we assume an off-axis detector such that the scattering vectors $\mathbf{q}$ in the detector are large compared to the $\mathbf{g}$ and $\mathbf{h}$ in the probe forming aperture. An off-axis detector satisfying this constraint is preferred in atomic resolution phonon spectroscopy [6]. We can then make the approximations that

$$\big[(\mathbf{q}-\mathbf{h})\cdot\boldsymbol{\varepsilon}^{\kappa}_{j'}\big]\big[(\mathbf{q}-\mathbf{g})\cdot\boldsymbol{\varepsilon}^{\kappa}_{j'}\big] \approx \big(\mathbf{q}\cdot\boldsymbol{\varepsilon}^{\kappa}_{j'}\big)^2 \tag{10}$$

and

$$\tilde{f}^{\kappa}_{e}(\mathbf{q}-\mathbf{h})\tilde{f}^{\kappa}_{e}(\mathbf{q}-\mathbf{g}) \approx \big[\tilde{f}^{\kappa}_{e}(\mathbf{q})\big]^2. \tag{11}$$

Then summing over all final states j' we obtain

$$\begin{aligned} &\sum_{j'}H^{*}_{(1j')0}(\mathbf{q}-\mathbf{h})H_{(1j')0}(\mathbf{q}-\mathbf{g}) \\ &\quad\approx \frac{h^5}{8\pi m^2}\sum_{\kappa}\exp[-2\pi i(\mathbf{g}-\mathbf{h})\cdot\mathbf{R}_{\kappa}]\big[\tilde{f}^{\kappa}_{e}(\mathbf{q})\big]^2 \\ &\quad\times\sum_{j'}\frac{1}{\omega_{j'}}\big(\mathbf{q}\cdot\boldsymbol{\varepsilon}^{\kappa}_{j'}\big)^2. \end{aligned} \tag{12}$$

Now

$$\begin{aligned} \sum_{j'}\frac{1}{\omega_{j'}}\big(\mathbf{q}\cdot\boldsymbol{\varepsilon}^{\kappa}_{j'}\big)^2 &= q^2\int d\omega\frac{1}{\omega}\sum_{j'}\delta(\omega-\omega_{j'})\big(\hat{\mathbf{q}}\cdot\boldsymbol{\varepsilon}^{\kappa}_{j'}\big)^2 \\ &= q^2\int d\omega\frac{1}{\omega}g^{\kappa}(\omega,\hat{\mathbf{q}}), \end{aligned} \tag{13}$$

where the quantity

$$g^{\kappa}(\omega,\hat{\mathbf{q}}) \equiv \sum_{j'}\delta(\omega-\omega_{j'})\big(\hat{\mathbf{q}}\cdot\boldsymbol{\varepsilon}^{\kappa}_{j'}\big)^2 \approx g^{\kappa}(\omega) \tag{14}$$

is the PDOS projected onto the atom κ along the direction of the unit vector $\hat{\mathbf{q}}$. In an isotropic system we can assume that the PDOS is independent of the direction defined by $\hat{\mathbf{q}}$ and, as indicated in Eq. (14), we have a contribution of $g^{\kappa}(\omega)$ for each in-plane direction for the PDOS projected onto the atom κ.

Therefore, we can write Eq. (12) as

$$\begin{aligned} &\sum_{j'}H^{*}_{(1j')0}(\mathbf{q}-\mathbf{h})H_{(1j')0}(\mathbf{q}-\mathbf{g}) \\ &\quad\approx \frac{h^5}{8\pi m^2}\sum_{\kappa}\exp[-2\pi i(\mathbf{g}-\mathbf{h})\cdot\mathbf{R}_{\kappa}]\big[\tilde{f}^{\kappa}_{e}(\mathbf{q})\big]^2 \\ &\quad\times q^2\int d\omega\frac{1}{\omega}g^{\kappa}(\omega). \end{aligned} \tag{15}$$

Differentiating Eq. (15) with respect to ω, and referring back to Eq. (3), we can write an inelastic differential cross section for single phonon excitation as a function of frequency ω as follows:

$$\begin{aligned} \frac{I(\mathbf{R},\omega)}{d\omega} &\approx \frac{\pi h}{2\omega k_0^2}\sum_{\kappa}g^{\kappa}(\omega)\int_{D}\big[\tilde{f}^{\kappa}_{e}(\mathbf{q})\big]^2 q^2\,d\mathbf{q} \\ &\times\iint\Psi_0^{*}(\mathbf{R},\mathbf{h})\Psi_0(\mathbf{R},\mathbf{g}) \\ &\times\exp[-2\pi i(\mathbf{g}-\mathbf{h})\cdot\mathbf{R}_{\kappa}]\,d\mathbf{h}\,d\mathbf{g}, \end{aligned} \tag{16}$$

where we have used $k_n \approx k_0$. The last two lines of Eq. (16) are the inverse Fourier transform of $|\Psi_0(\mathbf{R},\mathbf{R}_{\kappa})|^2$, so that it reduces to the simple and intuitive form

$$\frac{I(\mathbf{R},\omega)}{d\omega} \approx \frac{\pi h}{2\omega k_0^2}\sum_{\kappa}|\Psi_0(\mathbf{R},\mathbf{R}_{\kappa})|^2 g^{\kappa}(\omega)\int_{D}\big[\tilde{f}^{\kappa}_{e}(\mathbf{q})\big]^2 q^2\,d\mathbf{q}. \tag{17}$$

This frequency-dependent cross section describes the energy-loss spectrum for a given probe position $\mathbf{R}$. The shape of the spectrum is determined by the projected PDOS of each atom and is further modulated by the $1/\omega$ term. The contribution of each atom is weighted by the intensity of the probe $|\Psi_0(\mathbf{R},\mathbf{R}_{\kappa})|^2$ at the atomic position $\mathbf{R}_{\kappa}$ for a given probe position $\mathbf{R}$. This $\mathbf{R}$-dependent admixture from different atomic sites allows the spectrum to change in both shape and amplitude when scanning the probe across the sample, in particular when atoms of different types are present. The contribution to the signal from an atom κ is also determined by the term integrating over the detector in Eq. (17). Referring back to Eq. (8), we remind ourselves that this term depends on the detector geometry, the electron scattering factor, the mass of the atom and a DWF as defined in Eq. (7).

At this point we account for the effect due to a finite temperature of the sample $T > 0$ K, where phonon modes can be occupied. This is achieved by modifying Eq. (17) as follows [30]:

$$\begin{aligned} \frac{I(\mathbf{R},E)}{dE} &\approx \frac{h^2}{4Ek_0^2}\frac{\exp(E/k_BT)}{\exp(E/k_BT)-1} \\ &\times\sum_{\kappa}|\Psi_0(\mathbf{R},\mathbf{R}_{\kappa})|^2 g^{\kappa}(E)\int_{D}\big[\tilde{f}^{\kappa}_{e}(\mathbf{q})\big]^2 q^2\,d\mathbf{q}. \end{aligned} \tag{18}$$

In Eq. (18) we have formulated the differential cross section in terms of the phonon energy $E = \omega/\hbar$. We also note that $g^{\kappa}(E) = g^{\kappa}(\omega)/\hbar$. The additional, temperature-dependent factor applies to a description of single-phonon excitation processes leading to an energy loss of the probing electron that corresponds to the phonon energy. A different factor applies for de-excitation processes leading to energy gain, respectively.

For its application it is useful to write Eq. (18) in the form

$$\frac{I(\mathbf{R},E)}{dE} \approx F_T(E)\sum_\kappa \alpha^\kappa(\mathbf{R})g^\kappa(E), \tag{19}$$

where

$$F_T(E) = \frac{h^2}{4Ek_0^2}\frac{\exp(E/k_BT)}{\exp(E/k_BT)-1} \tag{20}$$

and

$$\alpha^\kappa(\mathbf{R}) = |\Psi_0(\mathbf{R},\mathbf{R}_\kappa)|^2 \int_D \left[\tilde{f}_e^\kappa(\mathbf{q})\right]^2 q^2\, d\mathbf{q}. \tag{21}$$

The factor $F_T(E)$, as given by Eq. (20), modulates the shape of the energy-loss spectrum relative to the shape of the PDOS. In general, intensities at low energy losses are amplified. Equation (21) makes clear that, when the STEM probe is at position $\mathbf{R}$, the contribution to the spectrum from atom κ is determined by the weighting function $\alpha^\kappa(\mathbf{R})$.

III. EXAMPLE

Now let us illustrate the use of Eq. (19) by applying it to the experimental work of Xu *et al.* on single-atom vibrational EELS [13]. They used a 60 keV STEM probe with a probe forming aperture of 32 mrad and an off-axis detector with a 12 mrad acceptance angle placed just outside the bright field disk. This tests the limit of the approximation relying on an EELS detector placed sufficiently off-axis such that the $\mathbf{q}$ in the detector are large compared to the $\mathbf{g}$ and $\mathbf{h}$ in the probe forming aperture. Initially we focus on the phonon spectral data for a Si-C$_3$ defect in graphene shown in Fig. 2(e) in Ref. [13]. The impurity Si atom can be slightly out of plane compared to the graphene layer, which is not expected to significantly affect the inelastic electron scattering and the following analysis. The theoretical calculations by Xu *et al.* have also not indicated a major influence of buckling of the Si-C$_3$ configuration on the phonon properties. In the projected structure, as shown in Fig. 1(a), the nearest-neighbor C atoms (labeled "1st C") and next-nearest neighbors (labeled "2nd C") to the Si atom are distinguished from the remaining C atoms of the graphene lattice as groups with different vibrational properties.

The measured energy-loss spectrum is obtained by scanning the probe over several probe positions $\mathbf{R}$ in an area in the vicinity of the Si atom, indicated schematically by the orange circles in Fig. 1. In each panel of Fig. 1 we plot the quantity $\alpha^\kappa(\mathbf{R})$ defined in Eq. (21), which shows, in the case of a spectrum recorded from the Si atom, that contributions to the signal can also come from surrounding atoms, especially those designated as 1st C. So, denoting the Si atom by κ', we can write an expression, using Eq. (19), for the measured spectrum integrated over the probe positions in the orange circle, taking into account the contribution from all atoms κ, as

$$\frac{I^{\kappa'}(E)}{dE} = F_T(E)\sum_\kappa \beta^{\kappa',\kappa}g^\kappa(E), \tag{22}$$

where

$$\beta^{\kappa',\kappa} = \int_{\kappa'} \alpha^\kappa(\mathbf{R})\, d\mathbf{R}. \tag{23}$$

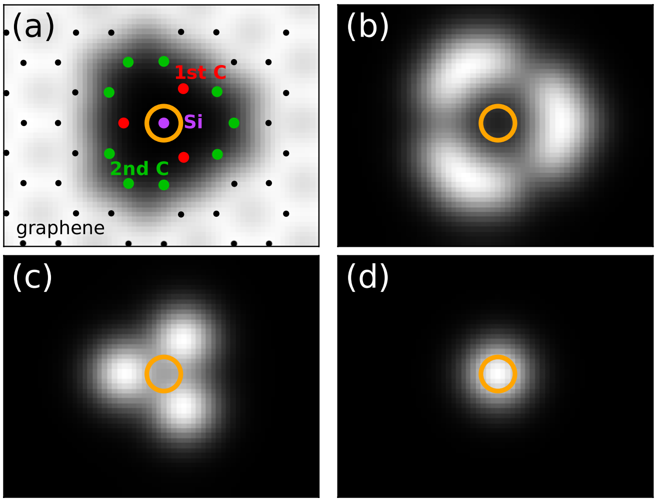

FIG. 1. (a) Si-C$_3$ impurity in graphene, with nearest neighbors to the Si atom designated 1st C and next-nearest-neighbors 2nd C. The atomic positions are indicated by dots in a super cell of size 12.78 Å × 9.84 Å in the plane of projection. The background is the quantity $\alpha^\kappa(\mathbf{R})$ defined in Eq. (21) for the atoms designated as graphene (black dots). (b) $\alpha^\kappa(\mathbf{R})$ for 2nd C atoms at positions marked in panel (a) by green dots. (c) $\alpha^\kappa(\mathbf{R})$ for 1st C carbon atoms (red dots). (d) $\alpha^\kappa(\mathbf{R})$ for the Si atom (purple dot). Each $\alpha^\kappa(\mathbf{R})$ is plotted on its own gray scale. The orange circle is centered at the Si position and indicates the applied integration area. The maps are calculated by scanning a 60 keV STEM probe with 32 mrad probe semi-convergence angle. The effect of a finite source size of 1 Å (HWHM) is included by convolution with a Gaussian distribution function.

In Eq. (23) the κ' notation for the area of integration implies integration over the orange circle in Fig. 1(a), which is centered on the atom κ', the Si atom in this case. The important feature of Eq. (22) is that it allows for a contribution to the measured signal from surrounding atoms, in other words for atoms with $\kappa \neq \kappa'$.

To facilitate a comparison between experimental and theoretical data for the Si-C$_3$ defect in Ref. [13], including possible linear combinations of calculated PDOS projected on individual atoms, we recast Eq. (22) in the following form:

$$\frac{\tilde{I}^{\kappa'}(E)}{dE} = \frac{1}{F_T(E)}\frac{I^{\kappa'}(E)}{dE} = \sum_\kappa \beta^{\kappa',\kappa}g^\kappa(E). \tag{24}$$

For a given experiment the function $F_T(E)$, defined by Eq. (20), is known. Therefore, we can process the experimentally measured energy-loss spectrum by multiplying by its inverse. We see that the experimental data, processed in this way, is a linear sum of $g^\kappa(E)$ contributing to the spectral data taken in the vicinity of a particular atom. As an aside, we note that applying the reciprocal factor $1/F_T(E)$ to the energy-loss spectrum is numerically more stable than applying $F_T(E)$ to the weighted sum of projected PDOSs in Eq. (22), since a division by small energy losses E is avoided. The fundamental quantities of interest are the projected PDOSs, an advantage of working with the processed data in Eq. (24).

There are two ways to proceed. First, we can use calculated PDOSs $g^\kappa(E)$ projected onto the atoms κ and then calculate

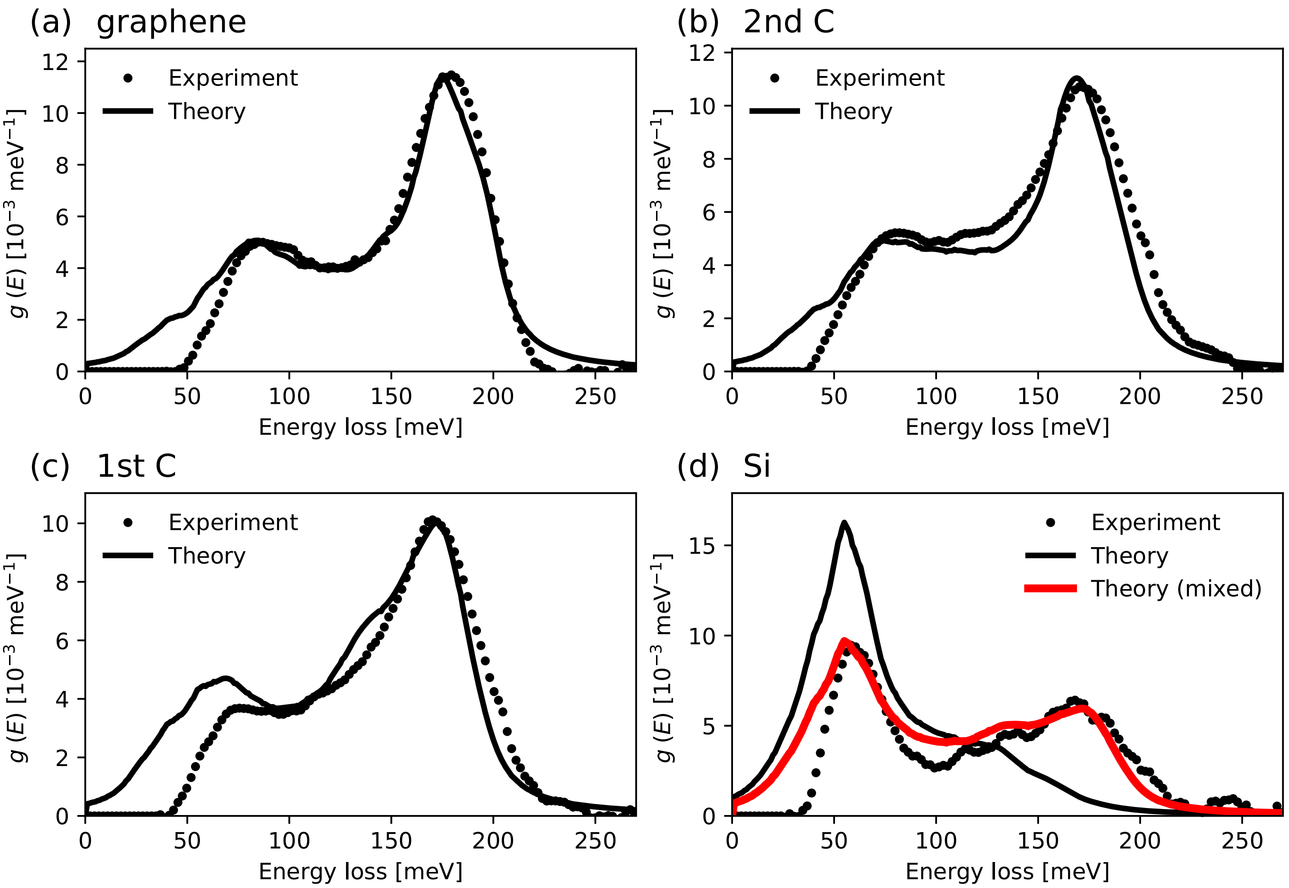

FIG. 2. Experimental energy-loss data (black dots) from Xu *et al.* [13] [Fig. 2(e)] for probe positions (a) on graphene, (b) on 2nd C atoms, (c) on 1st C atoms, and (d) on the Si impurity after processing per Eq. (24) by applying the factor $1/F_T(E)$. Theoretical projected phonon densities of states (black curves) from Ref. [13] [Fig. 2(f)] are plotted after normalization as $\int g^\kappa(E)\,dE = 1$. For the case of Si in panel (d) a contribution from 1st C atoms is assumed in a mixed density of states (thicker red curve) with $0.55g^{\mathrm{1stC}}(E) + 0.45g^{\mathrm{Si}}(E)$. Experimental results have been scaled for comparison to the theory and to the mixed result in panel (d).

the quantities on the right-hand side (r.h.s.) of Eq. (24) to compare with processed experimental data on the left-hand side (l.h.s.) of Eq. (24). The second possibility is that, since Eq. (24) is a linear system of equations, it can be inverted at each energy loss to obtain the separate $g^\kappa(E)$ per atom from experiment. This assumes, that the coefficients $\beta^{\kappa',\kappa}$ can be calculated based on prior knowledge of some experimental parameters and the atomic structure, including a good estimate for the MSD $\langle u^2_{x,T}\rangle^\kappa$ of each atom. In the following we apply the first approach to the EELS results recorded by Xu *et al.* [13] and compare this to their calculated PDOS data. We then demonstrate how the second approach can be applied to remove mixing from EELS data and compare these results also to the calculations by Hage *et al.* [10].

For the Si-C$_3$ impurity that we have been discussing, we obtain results as shown in Fig. 2. In each case the probe was positioned in the vicinity of atoms of the type/group indicated. We see in Fig. 2(a) that the processed experimental data corresponding to the l.h.s. of Eq. (24) agrees well with the calculated PDOS projected onto a single C atom in pristine graphene over the full available range of energy losses. Good qualitative agreement is also obtained for the 2nd and 1st C atoms surrounding the Si impurity. Some discrepancy in the vicinity of the energy-loss ranges <50 meV and >200 meV used for EELS background estimation and subtraction are expected. In Fig. 2(b) we see that for the 2nd C atoms the discrepancy between experiment and theory may be indicative of some mixing from 1st C atoms. Figure 2(c) shows that, when the probe is in the vicinity of a 1st C atom, a discrepancy between experiment and theory is more evident. However, with the probe in the vicinity of the Si atom, it is completely clear that experiment and theory are in disagreement between 100 to 200 meV. This disagreement was not so obvious when comparing energy-loss spectra with calculated PDOS projected on this atom, as presented by Xu *et al.* [13]. When processing the experimental data via Eq. (24), to put them in the form of a linear combination of projected PDOSs, the factor in $1/F_T(E)$, cf. Eq. (20), enhances the processed data with respect to the original energy-loss data for larger E. It is not sufficient to consider only the contribution from $g^{\mathrm{Si}}(E)$ to describe the processed data acquired in the vicinity of the Si impurity.

As already discussed, when the probe is scanned in the vicinity of the Si atom indicated by the orange circle in Fig. 1, the tails of the probe are also interacting with the set of three 1st C atoms. Figure 2(d) shows a much better agreement between theory and experiment for a mixing given by the linear combination $0.55g^{\mathrm{1stC}}(E) + 0.45g^{\mathrm{Si}}(E)$, with

TABLE I. Mixing parameters $\beta^{\kappa',\kappa}$, $\kappa' = \mathrm{Si}$.

$\kappa = \mathrm{Gr}$	$\kappa = \mathrm{2nd\ C}$	$\kappa = \mathrm{1st\ C}$	$\kappa = \mathrm{Si}$
0.03	0.18	0.35	0.44

projected PDOS data as provided in Ref. [13] and normalized as $\int g^{\kappa}(E)\,dE = 1$ on each atom, for consistency with the theory presented here. We note that the theoretical PDOS data provided by Xu *et al.* [13] are normalized to take into account the number of 1st C atoms (three in this case) and the number of 2nd C atoms (nine), while the normalization for graphene and Si are for single atoms.

Let us now investigate whether the mixing applied to achieve an agreement with the experimental data in Fig. 2(d) can be further justified. From Supplemental Material Fig. S7(b) of Ref. [13], we estimate that the radius of the integration area for the signal on the Si atom is 0.7 Å. In reality, the ideal probe implied by a probe-forming aperture of 32 mrad has aberrations, e.g., defocus and twofold astigmatism and there is also some spatial incoherence. We have taken this into account in a global way by convolving the probe with a Gaussian function of 1 Å half width at half maximum (HWHM). We have then calculated the quantities $\alpha^{\kappa}(\mathbf{R})$ in Eq. (21) as displayed in Fig. 1 for each group of atoms in the defect structure indicated in Fig. 1(a). It is clear that integration over the area around the Si atom, the orange circle in each case, yields a nontrivial contribution to the signal, in particular from atoms designated 1st C, and only to a lesser degree from the other groups of C atoms. The estimated values of $\beta^{\kappa',\kappa}$, summed over all atoms in each group, are listed in Table I.

The applied mixing is consistent with the weights listed in Table I when assigning the sum of all C weights (0.56) to the 1st C atoms. In other words, assuming a contribution from 1st C atoms only, there is an additional effective component included that mocks up the contribution from graphene and 2nd C atoms. In fact, due to the similarity of the PDOS projected on the different C groups, the summed PDOS using all four weights in Table I is very close to the curve assuming an admixture of only 1st C atoms with weight 0.55 in Fig. 2(d) and an additional plot is not warranted.

In Fig. 3 we consider some of the experimental energy loss data shown in Figs. 2(b) and 4(b) in Xu *et al.* [13]. Once again this has been processed as per Eq. (24). Figure 3(a) shows the results for the probe nominally in the vicinity of the Si atom for a Si-C$_4$ impurity. The linear combination $0.6g^{\mathrm{1stC}}(E) + 0.4g^{\mathrm{Si}}(E)$, with the theoretical projected PDOS normalized to unity, again achieves a better agreement over a wide energy loss range than the theoretical curve calculated for the Si atom alone. However, an unexplained difference between experiment and theory remains in the region >200 meV.

Figure 3(b) shows processed results for an N atom in an N-C$_3$ impurity. We have again mixed in a contribution from the 1st C atoms as $0.67g^{\mathrm{1stC}}(E) + 0.33g^{\mathrm{N}}(E)$, obtaining a better agreement between theory and experiment than for the calculated PDOS projected on the N atom only. The point to note is that this causes a shift in the position of the main peak, bringing it into better alignment with the experimental observation and also considerably improves agreement between experiment and theory to the right of the peak. We note that processing the data moved a peak at 157 to 165 meV (mainly a consequence of a multiplication by E). The peak in $g^{\mathrm{N}}(E)$ is at 155 meV but in the mixed PDOS it is at 161 meV.

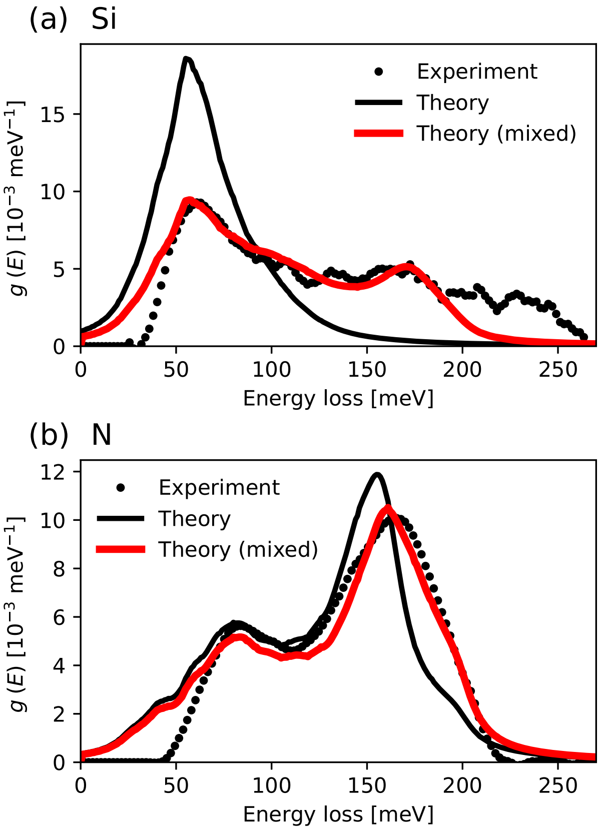

FIG. 3. Processed energy-loss data (black dots) from Figs. 2(b) and 4(b) in Xu *et al.* [13] with the probe in the vicinity of the impurity atom for each defect. Panel (a) is for the Si atom in a Si-C$_4$ impurity and (b) an N atom in an N-C$_3$ impurity. The theoretical projected phonon density of states from Ref. [13] is shown in each case (black curves). The experimental data is further compared with a linear combination of densities of states including a contribution from 1st C atoms. In panel (a) this combination is $0.6g^{\mathrm{1stC}}(E) + 0.4g^{\mathrm{Si}}(E)$ (thicker red curve), in panel (b) we have assumed $0.67g^{\mathrm{1stC}}(E) + 0.33g^{\mathrm{N}}(E)$. Theoretical results are normalized as $\int g^{\kappa}(E)\,dE = 1$. Experimental results are scaled for comparison with the mixed result in each case.

An inversion of the mixing approach as applied above can be formulated by making use of the linear relations between the preprocessed EELS data on the l.h.s. and the PDOS projected on individual atom (types) on the r.h.s. of Eq. (24). This set of linear equations can be inverted by multiplying both sides by the inverse of the matrix $\boldsymbol{\beta}$ formed by the coefficients $\beta^{\kappa',\kappa}$. We can thus write Eq. (24) and its inversion in matrix form as

$$\frac{\tilde{\mathbf{I}}(E)}{dE} = \boldsymbol{\beta}\,\mathbf{g}(E), \tag{25}$$

$$\mathbf{g}(E) = \boldsymbol{\beta}^{-1}\frac{\tilde{\mathbf{I}}(E)}{dE}, \tag{26}$$

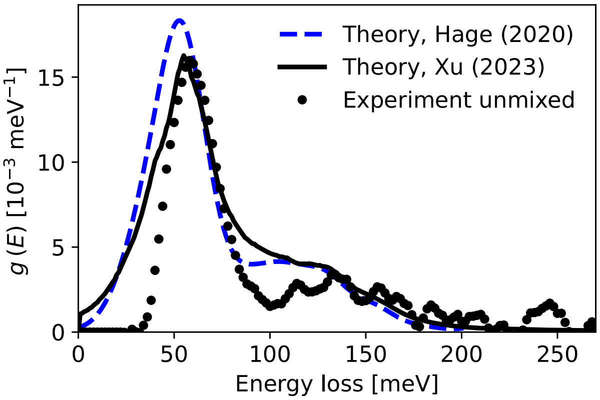

FIG. 4. PDOS projected on the single Si atom as extracted from the experimental data by unmixing (dots) and compared to the theoretical calculations in Refs. [10,13] (curves).

with vectors $\tilde{\mathbf{I}}(E)/dE$ representing the processed EELS data for each integration area κ' in the 2D EELS scan, and $\mathbf{g}(E)$ is the list of projected PDOSs for all contributing atoms κ.

For demonstration purpose, we consider the mixing factors used previously for the results shown in Fig. 2(d), which effectively is just a two-dimensional problem of mixing Si and 1st C PDOSs to compare to the EELS data recorded on the Si position. The respective two-dimensional matrix $\boldsymbol{\beta}$ and its inverse are

$$\boldsymbol{\beta} = \begin{pmatrix} 0.45 & 0.55 \\ 0.0 & 1.0 \end{pmatrix} \text{ and } \boldsymbol{\beta}^{-1} = \begin{pmatrix} 2.22 & -1.22 \\ 0.0 & 1.0 \end{pmatrix}, \quad (27)$$

with the system set up such that the first item of each vector corresponds to Si and the 2nd to 1st C.

The Si PDOS obtained from applying this unmixing procedure to the experimental EELS data is plotted in Fig. 4 and compared to the respective theoretical results taken from Hage *et al.* [10] and Xu *et al.* [13]. The theoretical PDOS of Hage *et al.* has been smoothed by an energy distribution with a width of 18 meV (FWHM), corresponding to the smoothing applied by Xu *et al.* to accommodate the energy resolution of their experiment. Both theoretical calculations agree reasonably well with the experiment in the energy-loss range where artifacts from background subtraction are expected to be minimal. An exception is the region around 100 meV, where both calculations somewhat overestimate the experimental PDOS data, with the result obtained by Hage *et al.* agreeing slightly better.

IV. DISCUSSION AND CONCLUSIONS

We have introduced a theory of phonon spectroscopy in atomic resolution STEM which explicitly includes the dependence on probe position in the inelastic scattering cross section itself and considers the contribution to the spectrum from individual atoms. This caters for a change of shape in the spectrum as a function of probe position for specimens containing different atomic species. The approach presented facilitates a more direct comparison between energy-loss spectra and PDOSs and suggests how one might deduce PDOSs projected on single atoms from experimental EELS data. Multiple scattering of the electron probe was not taken into account here. We expect that this effect can modify the mixing factors of the individual atomic contributions of thicker samples to vibrational STEM-EELS data in a nontrivial way, leading to complications for an analysis aiming at atomic-scale resolution. However, this effect can be neglected for very thin samples, such as for the impurities in single-layer graphene discussed here, for which single electron scattering will clearly dominate.

For an atomic-scale probe nominally in the vicinity of a particular atom, we have demonstrated that contributions to a spectrum from surrounding atoms due to the probe spreading can be significant and are important for correctly modeling the shape of a spectrum and also when using peak positions as an analytical tool. Nevertheless, roughly speaking, mainly one atom at a time is illuminated by the probe such that the interference effects between atoms are likely small and the assumption of atoms contributing incoherently is reasonable. Furthermore, the integration of interference terms over a large detector area usually leads to further cancellations.

It is interesting to note that integrating Eq. (17) over frequency ω yields an expression for the inelastic scattering cross section at the probe position $\mathbf{R}$ which is proportional to atomic MSDs. A similar result is obtained in the context of an Einstein model [29] and this has been used in a much simpler model for vibrational EELS [30]. Once we are at the level of MSDs, the information that is contained in a correlated phonon model and encapsulated in the projected PDOS on individual atoms is no longer evident. Furthermore, our assumption here that different atoms contribute incoherently to the scattering cross section is inherent in the Einstein model and the convergence of the two approaches is not unexpected. Nevertheless, the Einstein model is successful in predicting cross sections integrated over energy loss [22]. This is a further argument supporting our assumption of incoherent contributions from different atoms made in the present model.

Another key assumption is that we have an EELS detector placed sufficiently far off-axis. This assumption, together with that of incoherent contributions from different atoms, has allowed us to arrive at an approach where we do not have to consider the details of phonon modes in the dispersion surfaces but where a PDOS projected onto each atom suffices.

Further investigations could be undertaken to check whether the approximations in our model are still reasonable under more general circumstances, such as in a multislice approach for a sample that is tens of nanometers thick and that would take into account multiple elastic scattering of the probe, which may become significantly dispersed. This could pave the way toward extracting projected PDOSs at atomic resolution for thicker specimens. Deconvolution of the multiple scattering of the probe to obtain projected PDOSs per atom could be possible similarly to how this was done for core-loss EELS [38], because Eq. (17) is structurally similar to the simulation of inner-shell EELS in terms of a local potential that represents the inelastic scattering [39]. The dependence on the z coordinate, which has been omitted here for better clarity, needs to be taken into account when describing the dynamics of multiple elastic scattering of the probe in a thicker sample and the possible structural differences of atomic planes perpendicular to the incident beam direction for more complex crystals. A prerequisite of this approach is knowledge of the atomic structure, sample thickness and other experimental parameters. Although the target of the deconvolution is to determine the projected PDOS of each atom type, a good *a priori* estimate of the related mean-square displacements would also be needed.

[1] O. L. Krivanek, T. C. Lovejoy, N. Dellby, T. Aoki, R. W. Carpenter, P. Rez, E. Soignard, J. Zhu, P. E. Batson, M. J. Lagos, R. F. Egerton, and P. A. Crozier, Vibrational spectroscopy in the electron microscope, Nature (London) **514**, 209 (2014).

[2] C. Dwyer, T. Aoki, P. Rez, S. L. Y. Chang, T. C. Lovejoy, and O. L. Krivanek, Electron-beam mapping of vibrational modes with nanometer spatial resolution, Phys. Rev. Lett. **117**, 256101 (2016).

[3] M. J. Lagos, A. Trügler, U. Hohenester, and P. E. Batson, Mapping vibrational surface and bulk modes in a single nanocube, Nature (London) **543**, 529 (2017).

[4] M. J. Lagos and P. E. Batson, Thermometry with subnanometer resolution in the electron microscope using the principle of detailed balancing, Nano Lett. **18**, 4556 (2018).

[5] J. A. Hachtel, J. Huang, I. Popovs, S. Jansone-Popova, J. K. Keum, J. Jakowski, T. C. Lovejoy, N. Dellby, O. L. Krivanek, and J. C. Idrobo, Identification of site-specific isotopic labels by vibrational spectroscopy in the electron microscope, Science **363**, 525 (2019).

[6] F. S. Hage, D. M. Kepaptsoglou, Q. M. Ramasse, and L. J. Allen, Phonon spectroscopy at atomic resolution, Phys. Rev. Lett. **122**, 016103 (2019).

[7] G. Radtke, D. Taverna, N. Menguy, S. Pandolfi, A. Courac, Y. Le Godec, O. L. Krivanek, and T. C. Lovejoy, Polarization selectivity in vibrational electron-energy-loss spectroscopy, Phys. Rev. Lett. **123**, 256001 (2019).

[8] R. Senga, K. Suenaga, P. Barone, S. Morishita, F. Mauri, and T. Pichler, Position and momentum mapping of vibrations in graphene nanostructures, Nature (London) **573**, 247 (2019).

[9] S. M. Collins, D. M. Kepaptsoglou, J. Hou, C. W. Ashling, G. Radtke, T. D. Bennett, P. A. Midgley, and Q. M. Ramasse, Functional group mapping by electron beam vibrational spectroscopy from nanoscale volumes, Nano Lett. **20**, 1272 (2020).

[10] F. S. Hage, G. Radtke, D. M. Kepaptsoglou, M. Lazzeri, and Q. M. Ramasse, Single-atom vibrational spectroscopy in the scanning transmission electron microscope, Science **367**, 1124 (2020).

[11] K. Venkatraman and P. A. Crozier, Role of convergence and collection angles in the excitation of long-and short-wavelength phonons with vibrational electron energy-loss spectroscopy, Microsc. Microanal. **27**, 1069 (2021).

[12] X. Yan, C. Liu, C. A. Gadre, L. Gu, T. Aoki, T. C. Lovejoy, N. Dellby, O. L. Krivanek, D. G. Schlom, R. Wu, and X. Pan, Single-defect phonons imaged by electron microscopy, Nature (London) **589**, 65 (2021).

[13] M. Xu, D.-L. Bao, A. Li, M. Gao, D. Meng, A. Li, S. Du, G. Su, S. J. Pennycook, S. T. Pantelides *et al.*, Single-atom vibrational spectroscopy with chemical-bonding sensitivity, Nat. Mater. **22**, 612 (2023).

[14] K. Venkatraman, B. D. Levin, K. March, P. Rez, and P. A. Crozier, Vibrational spectroscopy at atomic resolution with electron impact scattering, Nat. Phys. **15**, 1237 (2019).

[15] Y.-H. Li, R.-S. Qi, R.-C. Shi, J.-N. Hu, Z.-T. Liu, Y.-W. Sun, M.-Q. Li, N. Li, C.-L. Song, L. Wang, Z.-B. Hao, Y. Luo, Q.-K. Xue, X.-C. Ma, and P. Gao, Atomic-scale probing of heterointerface phonon bridges in nitride semiconductor, Proc. Natl. Acad. Sci. USA **119**, e2117027119 (2022).

[16] T. Lee, J. Qi, C. A. Gadre, H. Huyan, S.-T. Ko, Y. Zuo, C. Du, J. Li, T. Aoki, R. Wu *et al.*, Atomic-scale origin of the low grain-boundary resistance in perovskite solid electrolyte $Li_{0.375}Sr_{0.4375}Ta_{0.75}Zr_{0.25}O_3$, Nat. Commun. **14**, 1940 (2023).

[17] L. J. Allen and T. W. Josefsson, Inelastic scattering of fast electrons by crystals, Phys. Rev. B **52**, 3184 (1995).

[18] A. Amali and P. Rez, Theory of lattice resolution in high-angle annular dark-field images, Microsc. Microanal. **3**, 28 (1997).

[19] A. V. Martin, S. D. Findlay, and L. J. Allen, Model of phonon excitation by fast electrons in a crystal with correlated atomic motion, Phys. Rev. B **80**, 024308 (2009).

[20] B. D. Forbes, A. V. Martin, S. D. Findlay, A. J. D'Alfonso, and L. J. Allen, Quantum mechanical model for phonon excitation in electron diffraction and imaging using a Born-Oppenheimer approximation, Phys. Rev. B **82**, 104103 (2010).

[21] N. R. Lugg, B. D. Forbes, S. D. Findlay, and L. J. Allen, Atomic resolution imaging using electron energy-loss phonon spectroscopy, Phys. Rev. B **91**, 144108 (2015).

[22] B. D. Forbes and L. J. Allen, Modeling energy-loss spectra due to phonon excitation, Phys. Rev. B **94**, 014110 (2016).

[23] C. Dwyer, Prospects of spatial resolution in vibrational electron energy loss spectroscopy: Implications of dipolar scattering, Phys. Rev. B **96**, 224102 (2017).

[24] L. J. Allen, H. G. Brown, S. D. Findlay, and B. D. Forbes, A quantum mechanical exploration of phonon energy-loss spectroscopy using electrons in the aloof beam geometry, Microscopy **67**, i24 (2018).

[25] R. J. Nicholls, F. S. Hage, D. G. McCulloch, Q. M. Ramasse, K. Refson, and J. R. Yates, Theory of momentum-resolved phonon spectroscopy in the electron microscope, Phys. Rev. B **99**, 094105 (2019).

[26] P. Rez and A. Singh, Lattice resolution of vibrational modes in the electron microscope, Ultramicroscopy **220**, 113162 (2021).

[27] P. M. Zeiger and J. Rusz, Efficient and versatile model for vibrational STEM-EELS, Phys. Rev. Lett. **124**, 025501 (2020).

[28] P. M. Zeiger and J. Rusz, Frequency-resolved frozen phonon multislice method and its application to vibrational electron energy loss spectroscopy using parallel illumination, Phys. Rev. B **104**, 104301 (2021).

[29] P. M. Zeiger, J. Barthel, L. J. Allen, and J. Rusz, Lessons from the harmonic oscillator: Reconciliation of the frequency-resolved frozen phonon multislice method with other theoretical approaches, Phys. Rev. B **108**, 094309 (2023).

[30] J. Barthel, P. M. Zeiger, J. Rusz, and L. J. Allen, Simple model for phonon spectroscopy using fast electrons, Phys. Rev. B **109**, 184105 (2024).

[31] P. Brüesch, *Phonons: Theory and Experiments II: Experiments and Interpretation of Experimental Results* (Springer-Verlag, Berlin, 1986), Vol. 65.

[32] W. Coene and D. Van Dyck, Inelastic scattering of high-energy electrons in real space, Ultramicroscopy **33**, 261 (1990).

[33] C. Dwyer, Multislice theory of fast electron scattering incorporating atomic inner-shell ionization, Ultramicroscopy **104**, 141 (2005).

[34] L. J. Allen, A. J. D'Alfonso, and S. D. Findlay, Modelling the inelastic scattering of fast electrons, Ultramicroscopy **151**, 11 (2015).

[35] T. W. Josefsson and L. J. Allen, Diffraction and absorption of inelastically scattered electrons for *K*-shell ionization, Phys. Rev. B **53**, 2277 (1996).

[36] C. Dwyer, S. D. Findlay, and L. J. Allen, Multiple elastic scattering of core-loss electrons in atomic resolution imaging, Phys. Rev. B **77**, 184107 (2008).

[37] S. L. Dudarev, L.-M. Peng, and M. J. Whelan, Correlations in space and time and dynamical diffraction of high-energy electrons by crystals, Phys. Rev. B **48**, 13408 (1993).

[38] N. R. Lugg, M. J. Neish, S. D. Findlay, and L. J. Allen, Practical aspects of removing the effects of elastic and thermal diffuse scattering from spectroscopic data for single crystals, Microsc. Microanal. **20**, 1078 (2014).

[39] N. R. Lugg, M. Haruta, M. J. Neish, S. D. Findlay, T. Mizoguchi, K. Kimoto, and L. J. Allen, Removing the effects of elastic and thermal scattering from electron energy-loss spectroscopic data, Appl. Phys. Lett. **101**, 183112 (2012).